Investigations on bubbly two-phase flow in a constricted vertical pipe

Neumann-Kipping, M.; Bieberle, A.; Hampel, U.;

Investigations on bubbly two-phase flow in a constricted vertical pipe

Martin Neumann-Kipping[1], André Bieberle[2], Uwe Hampel[1,2]

[1] Chair of Imaging Techniques in Energy and Process Engineering, Technische Universität Dresden, 01062 Dresden, Germany

[2] Institute of Fluid Dynamics, Helmholtz-Zentrum Dresden - Rossendorf, Bautzner Landstraße. 400, 01328 Dresden, Germany

Abstract

We report on an experimental investigation of adiabatic bubbly two-phase flow development in a DN50 pipe with a ring-shaped and a baffle-shaped constriction at different superficial velocities of gas (up to j_g = 0.1400 m·s^{-1}) and liquid (up to j_l = 1.6110 m·s^{-1}) using ultrafast electron beam X-ray computed tomography (UFXCT). From UFXCT images, cross-sectional gas holdup distributions were obtained with a temporal resolution of up to 2,500 frames per second in 18 scanning planes along the pipe. A sophisticated data processing approach was applied to extract gas holdup data immediately from the two-phase flow image stack. Based on that, time-averaged gas holdup of the cross-section and the axial center of the pipe were calculated. In addition, bubble sizes and velocities were determined.

Key words: gas-liquid two-phase flow, bubbly flow, flow constriction, three-dimensional flow, computed tomography, experimental benchmark data

1 Introduction

Two-phase flows can be found in many industrial applications. Examples are multiphase chemical reactors, power plant circuits, heat exchangers or oil and gas production. Hence, there is a continuing interest in modelling and simulation. Computational fluid dynamics is the method of choice to simulate such flows at a high level of detail. However, for two-phase flow such simulation codes are yet not fully mature due to the inherent physical complexity of flows with phase boundaries. This holds especially for gas-liquid two-phase flow due to the deformability of gas-liquid interfaces. [1–3]. Thus, experimental validation is still inevitable. The particular challenge there, however, is the need to produce data with highest resolution in space and time, e.g. for transient flow phenomena.

Two phase flow in straight pipes of any inclination has been seen as a benchmark case for multiphase CFD for some years now. Hence, numerous experimental test cases are known from literature, e.g. for vertical upward flow [4–6], downward flow [7–9] or both flow directions [10–12], as well as horizontal flow [13–15]. A logical next step are benchmark cases for slightly more complex flow scenarios, such as constrictions, bends or junctions, with significant three-dimensional flow effects, such as flow separation at sharp edges, recirculation areas or curved streamlines. For the latter, however, only very few CFD-grade experimental data are available. One example is Prasser et al. [16] and Frank et al. [17], who investigated the flow around an axially moveable semicircular obstacle for a vertical pipe with an inner diameter of 195.3 mm using the wire-mesh sensor technique [18,19]. In these studies, the authors measured phase distributions and bubble sizes with a temporal resolution of 2,500 images per second for air-water and steam-water flow. From this, axial and lateral gas bubble velocities as well as time-averaged liquid velocities were estimated. The data was used for assessment and validation of CFD simulations with ANSYS CFX employing a multiple size group modelling approach for the gas phase [20]. The slight intrusiveness of the wire-mesh sensor

53 and the driving mechanism of the obstacle as well as the 3 mm spatial resolution
54 brought about increasing uncertainties for smaller bubbles and lower liquid
55 velocities [21,22]. The present study aimed at the extension of the available
56 experimental database for bubbly gas-liquid two-phase flow with a pronounced
57 three-dimensional flow field. Experiments have been performed in a vertical pipe
58 with an inner diameter of 53 mm. The impact of two different flow constrictions
59 on the flow field were studied: a baffle-shaped and a ring-shaped type,
60 respectively. The choice was made, because the baffle-shaped constriction creates
61 an asymmetric flow field while the ring-shaped one creates an axially symmetric
62 flow fields. This is useful to study different aspects of the flow, such as in-plane
63 flow components. Hence, some comparability to already existing experimental
64 data [16] is given for the baffle-shaped flow constriction. In addition, the ring-
65 shaped flow constriction provides a true extension of the available database.

66 Experiments were performed using ultrafast X-ray computed tomography (UFXCT)
67 [23,24]. It is a fast and non-invasive imaging technique for the investigation of
68 highly transient processes, especially for bubbly two-phase flows [11,25–29]. With
69 the applied temporal resolution of up to 2,500 images per second, the fluid
70 dynamics could be studied without influencing the flow field. With this imaging
71 technique we obtained quantitative parameters, such as total phase holdups,
72 cross-sectional phase distributions, gas bubble sizes as well as their distributions
73 and velocities. In the following we discuss only selected results. For access to the
74 full data set the reader is referred to the RODARE Open Data Link given in [30,31].

2   Experimental setup

75

76 *2.1   Vertical test section*

77 Experiments are conducted in a vertical test section at the thermal-hydraulic test
78 facility TOPFLOW (see Figure 1 a)) [30], [31]. Here, flow investigations have been
79 performed under adiabatic conditions in an acrylic pipe with an inner diameter of

80   D = 53 mm and a total length of L = 4950 mm. Deionized water and compressed

81   air were used as liquid and gas phase in co-current upward flow. Inlet flow rates

82   are controlled by a volute pump (HPH 100-250, KSB, Germany) and a mass flow

83   controller (F-202AC, Bronkhorst, Netherlands) for liquid and gas phase

84   respectively. With this equipment we maintain a constant liquid temperature of

85   30°C and pressure of 4 bar at the gas injection at the bottom of the test section.

86

87   a)   c)
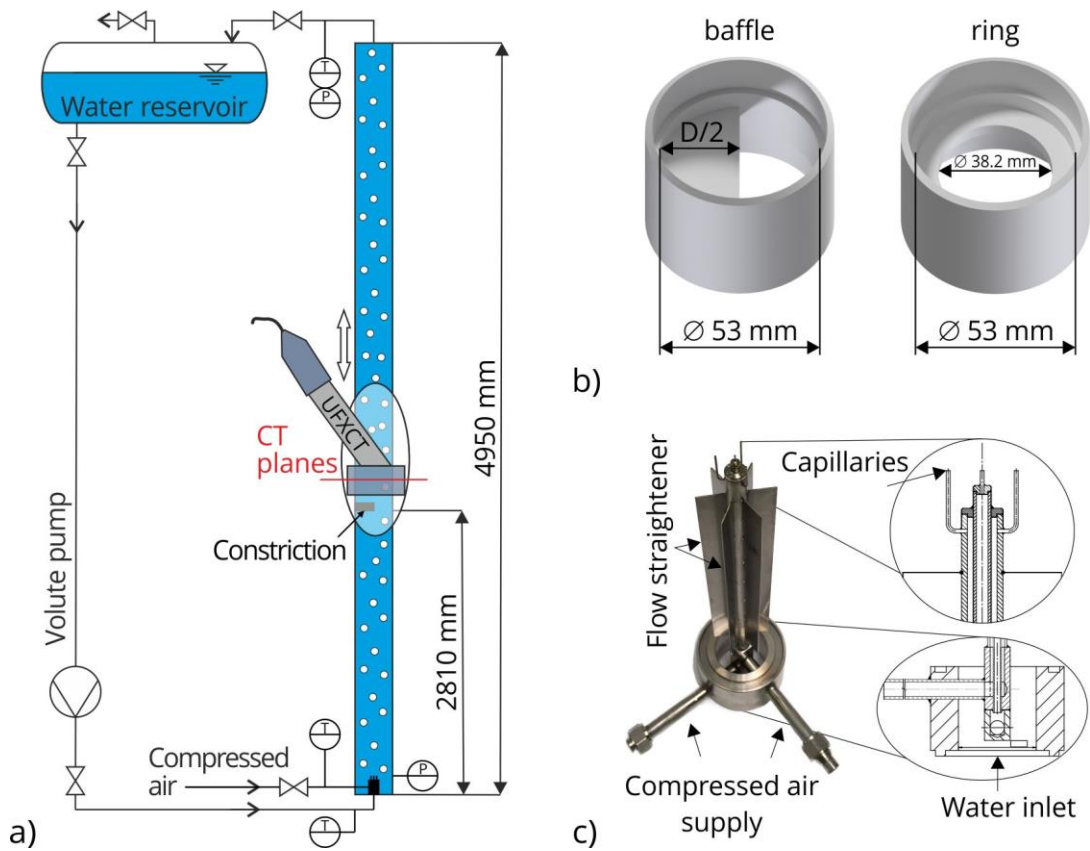
88   Figure 1:   Schematic representations of the vertical obstructed test section showing a) the entire
89   test section pipe connected to the (simplified and reduced depicted) TOPFLOW facility,
90   b) the applied flow constrictions for generation of three-dimensional flow fields and c)
91   the gas injection module.

92

93   Figure 1 b) shows both flow constrictions, the baffle-shaped and ring-shaped one.

94   Both block exactly half of the inner pipe cross-section. Each obstacle is 5 mm thick

95   and its bottom edge is at a distance of l = 2810 mm above the gas injector. That is,

4

96 we have a length-to-diameter ratio of l/D = 52, for which we consider the two-
97 phase flow as fully developed.

98 Figure 1 c) shows the gas injection module that was already used in previous
99 studies, e.g. Banowski et al. for comparability study of UFXCT and wire-mesh
100 sensor technique [22]. It mainly comprises four capillaries with an inner diameter
101 of 0.8 mm and six equidistantly arranged metal sheets for straightening and
102 homogenizing the liquid flow.

103

104 *2.2   Ultrafast X-ray computed tomography*

105 Ultrafast electron beam X-ray computed tomography (UFXCT) uses a deflected
106 electron beam to produce a rapidly rotating X-ray spot. Along with a stationary
107 multi-pixel dual-plane X-ray detector this configuration is used to scan
108 tomographic projections of the flow. From these, cross-sectional images are
109 reconstructed. Each image has a size of 180×180 pixels with a corresponding pixel
110 size of 0.5 mm. The in-plane spatial resolution of the UFXCT scanner is nominally
111 1 mm. However, since gas-liquid flow has a specific contrast, we found in earlier
112 studies that detection of single gas bubbles is secure only for bubbles with a
113 dimeter of d_B ≥ 2 mm. The two imaging planes of the UFXCT scanner offer a
114 geometric distance of about 10 mm. The imaging speed in this study was up to
115 2,500 frames per second and per plane, depending on the expected flow velocity.
116 For more details on general principles of computed tomography, the reader is
117 referred to [34–36] and for more details on ultrafast X-ray computed tomography
118 to [24,37,38].

119 The UFXCT scanner can be freely moved along the pipe with the help of an elevator
120 mechanism. Hence it is possible to study the gas-liquid flow in any position up- and
121 downstream of the flow constriction. The scanning planes used in this study are

122 compiled in Table 1 as distances z of the upper and lower imaging plane with
123 respect to the center of the flow constriction.

124

125 Table 1: Image plane identifiers along the vertical test section pipe and according distances z
126 of the upper and lower UFXCT imaging plane to the center of the respective flow
127 constriction. Additionally dimensionless distance-to-diameter ratios z/D are given.

Identifier	A	B	C	D	E	F	G	H	I
z [mm]	-200	-60	0	5	20	50	100	200	400
	-210	-70	-10	-5	10	40	90	190	390
z/D	-4	-1	0	0.1	0.5	1	2	4	8

128

129 *2.3   Gas holdup*

130 The raw tomographic data is a set of gray value images encoding the X-ray
131 attenuation coefficient $\mu_{i,j,k}$ of a pixel with indices (i,j) and temporal index k. The
132 conventional procedure to calculate gas holdup from UFXCT images is as follows:
133 scans of the two-phase flow $\mu_{i,j,k}^{(\mathrm{tp})}$ and two k-averaged reference states, i.e. empty
134 cross section $\bar{\mu}_{i,j}^{(\mathrm{gas})}$ and liquid filled cross section $\bar{\mu}_{i,j}^{(\mathrm{liq})}$, are used to calculate the
135 gas holdup $\varepsilon_{i,j,k}$ according to

$$\varepsilon_{i,j,k} = \frac{\bar{\mu}_{i,j}^{(\mathrm{liq})} - \mu_{i,j,k}^{(\mathrm{tp})}}{\bar{\mu}_{i,j}^{(\mathrm{liq})} - \bar{\mu}_{i,j}^{(\mathrm{gas})}}. \tag{1}$$

136 This method has already been introduced by Zalucky et al. [39]. However, it was
137 found that this method is sensitive to image artifacts from e.g. beam hardening,
138 radiation scattering and geometrical dispositions of the deflected X-ray source
139 and/or the object of investigation [40].

140 Therefore, an improved data processing procedure was developed. Here, the
141 liquid reference data set $\bar{\mu}_{i,j}^{(\mathrm{liq})}$ and an estimation of the attenuation difference

6

142    $\bar{\mu}_{i,j}^{(\text{liq})}$ - $\bar{\mu}_{i,j}^{(\text{gas})}$ are directly extracted from the two-phase flow data $\mu_{i,j,k}^{(\text{tp})}$. The

143   calculation comprises two main processing steps: a) a histogram calibration step

144   from which the liquid reference data set $\bar{\mu}_{i,j}^{(\text{liq})}$ is obtained and b) an optimization

145   step from which the attenuation difference $\bar{\mu}_{i,j}^{(\text{liq})}$ - $\bar{\mu}_{i,j}^{(\text{gas})}$ is estimated. This

146   approach effectively suppresses adverse effects of image artifacts and non-

147   linearities.

148   Figure 2 illustrates the first data processing step. Here, a histogram of all k

149   reconstructed attenuation values $\mu_{i,j,k}^{(\text{tp})}$ is compiled for each image pixel (i,j). If the

150   average gas holdup of the corresponding pixel (i,j) is around 50%, then its

151   attenuation value distribution is typically bimodal (see Figure 2, bottom center).

152   Though the gas and liquid phase in a two-phase flow have well-defined

153   attenuation coefficients, the reconstructed values are corrupted by noise, artifacts

154   and non-linearities. As the Poisson noise of the X-ray source and the Gaussian

155   noise of the detectors are dominating we can assume a Gaussian distribution for

156   both values. Hence, we extract average liquid $\mu_\mu^{(\text{liq})}$ and gas $\mu_\mu^{(\text{gas})}$ values from $\mu_{i,j,k}^{(\text{tp})}$

157   by fitting two Gaussian curves into the histogram. This is done for all image pixels.

158   As the liquid phase is dominant in our case of bubbly two-phase flow, $\mu_\mu^{(\text{liq})}$ can be

159   determined with good accuracy. For $\mu_\mu^{(\text{gas})}$ it is more difficult, as its peak in the

160   histogram is typically weak or even missing. Note, if gas phase would be dominate,

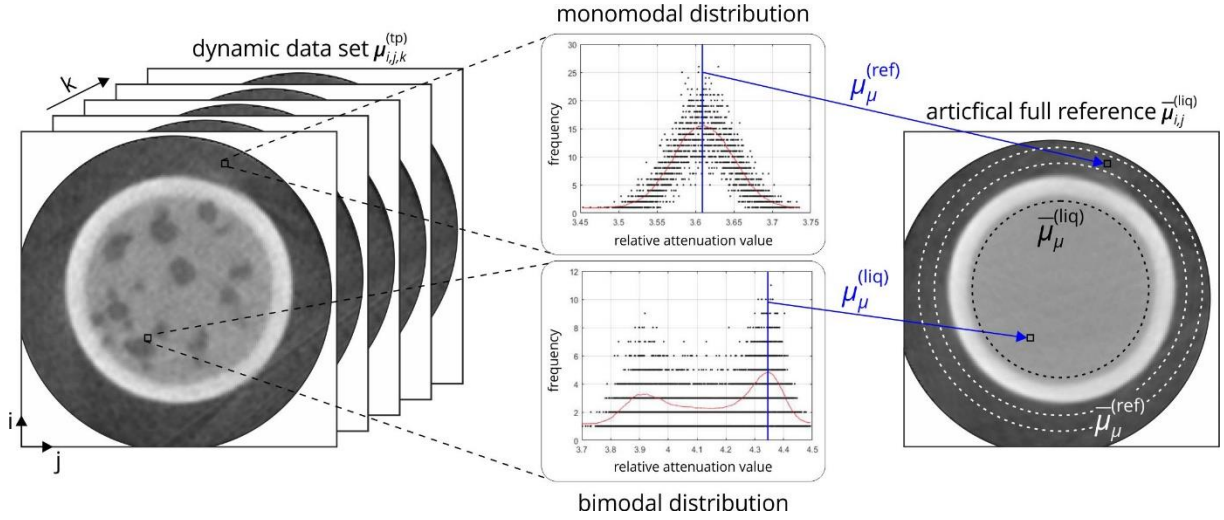161   e.g. for droplet flow, the situation would be vice versa.

162

Figure 2: Schematic illustration to extract a full reference data set $\bar{\mu}_{i,j}^{(\text{liq})}$ from the dynamic two-phase flow data set $\mu_{i,j,k}^{(\text{tp})}$ based on a frequency distribution analysis of attenuation values at each image pixel (i,j).

Thus, the attenuation difference $\bar{\mu}_{i,j}^{(\text{liq})} - \bar{\mu}_{i,j}^{(\text{gas})}$ is determined in a second data processing step. As illustrated in Figure 2 we may obtain $\bar{\mu}_{i,j}^{(\text{gas})}$ from reference pixels with average value $\bar{\mu}_{\mu}^{(\text{ref})}$ outside the column. However, as it can also be seen in Figure 2, the gas values in the bubble are on average slightly brighter which is caused by partial volume effects as well as beam scattering and beam hardening artifacts. Therefore, the sought value $\bar{\mu}_{i,j}^{(\text{gas})}$ is obtained in the following way.

We set $\bar{\mu}_{i,j}^{(\text{gas})} = \bar{\mu}_{\mu}^{(\text{ref})}$, calculate the gas holdup according to Eq. (1) and compile the histogram (left side of Figure 3). As can be seen, the gas holdup maximum is $\varepsilon < 1$ while we would expect it to be $\varepsilon = 1$. Now, we fit a Gaussian distribution function to the right slope of the histogram and determine its mean value ε_m. Now the task is to find an appropriate average attenuation value for gas, which is larger than the reference value by an offset a, that is

$$\bar{\mu}_{i,j}^{(\text{gas})} = \bar{\mu}_{\mu}^{(\text{ref})} + a \,. \tag{2}$$

If this reference value shifts ε_m to 1, as we would expect, then Eq. (1) can be written as

8

$$\frac{\varepsilon_{i,j,k}}{\varepsilon_m} = \frac{1}{\varepsilon_m} \frac{\bar{\mu}_{i,j}^{(liq)} - \mu_{i,j,k}^{(tp)}}{\bar{\mu}_{i,j}^{(liq)} - \bar{\mu}_{\mu}^{(ref)}} = \frac{\bar{\mu}_{i,j}^{(liq)} - \mu_{i,j,k}^{(tp)}}{\bar{\mu}_{i,j}^{(liq)} - \left(\bar{\mu}_{\mu}^{(ref)} + a\right)}. \tag{3}$$
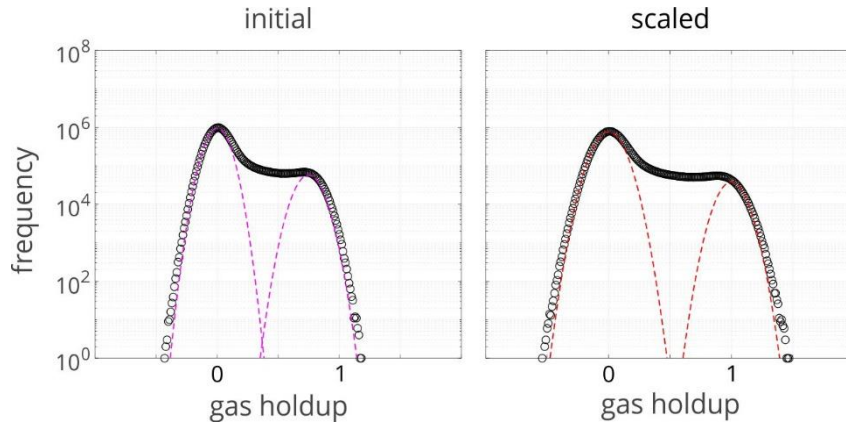
182   Setting $\Delta = \bar{\mu}_{i,j}^{(liq)} - \bar{\mu}_{\mu}^{(ref)}$ and solving for a yields

$$a = \Delta(1 - \varepsilon_m) \tag{4}$$

183   or by using Eq. (2)

$$\bar{\mu}_{i,j}^{(gas)} = (1 - \varepsilon_m)\bar{\mu}_{i,j}^{(liq)} + \varepsilon_m \bar{\mu}_{\mu}^{(ref)}. \tag{5}$$

184   With this value for $\bar{\mu}_{i,j}^{(gas)}$ we obtain the scaled histogram shown on the right side

185   of Figure 3.

186

187   Figure 3:   Gas holdup histogram calculated according to Eq. (1) using $\bar{\mu}_{\mu}^{(ref)}$ (left) and

188          $(1 - \varepsilon_m)\bar{\mu}_{i,j}^{(liq)} + \varepsilon_m \bar{\mu}_{\mu}^{(ref)}$ (right) as empty reference $\bar{\mu}_{i,j}^{(gas)}$.

189

190   *2.4   Gas phase parameters and bubble properties*

191   From the $\varepsilon_{i,j,k}$ we can calculate the time-averaged cross-sectional gas phase

192   distribution:

$$\bar{\varepsilon}_{i,j} = \frac{1}{N_k}\sum_{k=1}^{N_k} \varepsilon_{i,j,k} \tag{6}$$

193   as well as time- and space-averaged total gas holdup

9

$$\bar{\varepsilon} = \sum_{i=1}^{N_i} \sum_{j=1}^{N_j} w_{i,j} \cdot \bar{\varepsilon}_{i,j}. \tag{7}$$

194 Here $w_{i,j}$ are weights encoding the fraction of pixel area inside the pipe cross

195 section. In a next step, we binarize $\varepsilon_{i,j,k}$ in order to discriminate gas from liquid.

196 Thus, an iterative algorithm is applied which is based on a concept proposed by

197 Banowski et al. [41]. Here, pixel clusters are identified as connected objects based

198 on seed points of maximum gas holdup. This algorithm finally yields two data sets:

199 a) a binarized data set $\varepsilon_{i,j,k}^{(bin)}$ containing values "1" and "0" for gas and liquid phase

200 only and b) a corresponding identifier data set $\varepsilon_{i,j,k}^{(id)}$, containing individual bubble

201 numbers. Furthermore, the bubble property analysis module of the wire-mesh

202 sensor data processing software is used to extract bubble properties, e.g. bubble

203 size and its position [42].

204 In the image stack, the axial dimension is time k. Hence, the identified bubble

205 volume is given in mm²·ms. It is required to convert time into length measures,

206 hence bubble volume needs to be multiplied by the axial gas phase velocity. To

207 determine this velocity a cross-correlation function

$$F_{i,j,\Delta k} = \frac{\sum_{k=1}^{N_k} \varepsilon_{i,j,k}^{(low)} \cdot \varepsilon_{i,j,k}^{(up)}}{\sqrt{\sum_{k=1}^{N_k} \left(\varepsilon_{i,j,k}^{(low)}\right)^2 \cdot \sum_{k=1}^{N_k} \left(\varepsilon_{i,j,k}^{(up)}\right)^2}} \tag{8}$$

208 of the gas holdup is calculated for each pixel pair (i,j) of upper scanning plane

209 $\varepsilon_{i,j,k}^{(up)}$ and lower scanning plane $\varepsilon_{i,j,k}^{(low)}$ separately. The index Δk corresponds to the

210 time-shift $\Delta t = \Delta k / f$ with f being the image frequency per scanning plane. Then,

211 the axial gas phase velocity map $\bar{u}_{i,j}^{(ax)}$ is calculated using the maximum of the

212 cross-correlation function according to

$$\bar{u}_{i,j}^{(\text{ax})} = \frac{\Delta m_{i,j}}{\Delta k_{i,j}^{(\text{max})}} \cdot f \qquad \text{where} \qquad \Delta k_{i,j}^{(\text{max})} = \arg\max_{k}\left(F_{i,j,\Delta k}\right). \tag{9}$$

213 Here, the unequal distribution of the effective imaging plane distance of the UFXCT

214 scanner is taken into account by the distance map $\Delta m_{i,j}$ as introduced by

215 Neumann et al. [43]. This allows for a position-dependent calculation of bubble

216 sizes. This approach is typically valid only for unidirectional flow, which is, however,

217 not the case in areas around the flow constrictions and in recirculation zones.

218 Here, morphological bubble properties are utilized to estimate the bubble velocity

219 and, thus, the bubble size based on its Eötvös number and aspect ratio [11,22].

220 Furthermore, the bubble size distribution is given by the frequency of occurrence

221 of a respective size class according to

$$H^{(\text{bub})}\left(d_{B,n}\right) = \frac{\sum_b \varepsilon\left(B_b\right)}{\bar{\varepsilon}\cdot\Delta d_B} \qquad \text{with} \quad b \in \left\{1 \dots N_b \middle| d\left(B_b\right) \in d_{B,n}\right\}. \tag{10}$$

222 Here, the frequency of occurrence $H^{(\text{bub})}$ for bubble size class $d_{B,n}$ is defined as

223 gas holdup ratio of the sum $\sum_b \varepsilon\left(B_b\right)$ and the time- and space-averaged gas

224 holdup $\bar{\varepsilon}$, divided by bubble size class width Δd_B. The sum is given by each bubble

225 B_b with b being element of the total bubble number N_b and the restriction that

226 the bubble diameter of the respective bubble $d\left(B_b\right)$ belongs to bubble size class

227 $d_{B,n}$. In addition, an alternative representation of the bubble size distribution is

228 given by the probability density function (PDF) that is calculated by applying a

229 kernel density estimation with an interval width of 10%.

230 Furthermore, redistribution of gas and liquid phase lead to significant lateral

231 bubble movement, especially close to the flow constrictions. Therefore, the

232 transversal movement of each bubbles center of mass is directly tracked for

233 according cross-sectional images, which allows for the determination of its lateral

234 velocity. Subsequently, the lateral velocity field $\bar{u}_{i,j}^{(\text{lat})}$ is derived by void fraction

weighted time-averaging of the lateral velocity over each available bubble that crossed the imaging plane during scanning [16].

3 Results

At the beginning of each experiment, deionized water is heated up and circulated through the test section, using the volute pump. In parallel, the pressure is increased by injecting de-oiled gas to the test section until both temperature and pressure reaches stable conditions of 30°C and 4 bar respectively. Subsequently, specific operating conditions are set by adjusting the liquid and gas flow rates as defined by their respective superficial velocity (see Table 2). In total, fifteen steady state operating conditions within the bubbly flow regime are considered for each flow constriction, based on flow maps of Taitel et al. [44]. After a waiting period of about 30 min the UFXCT scans are performed at the different scanning heights, starting at position "A" (see Table 1), for a scanning interval of 15 s. The imaging frequency has been adapted corresponding to the expected flow velocity within the pipe (see Table 2) to obtain a sufficient number of images.

Experimental matrix for both flow constrictions based on various combinations of gas and liquid superficial velocities. Highlighted numbers identify the applied UFXCT image frequency f per scanning plane (blue: 1,000 Hz; green: 2,500 Hz).

j_g – gas superficial velocity

m·s^{-1}	0.0151	0.0368	0.0898	0.1400
1.6110	#053	#075	-	-
1.0170	#052	#074	#096	#107
0.4050	#050	#072	#094	#105
0.1020	#047	#069	#091	-
0.0405	#045	#067	-	-

j_l – liquid superficial velocity

As a first analyzing step, the initial flow conditions for each flow constrictions and operating condition are compared. Therefore, the total gas holdup values $\bar{\varepsilon}$ of the four furthest upstream imaging planes (upper and lower UFXCT imaging plane for scanning positions "A" and "B") are compared as the two-phase flow is here undisturbed and fully developed. The corresponding parity plot in Figure 4 shows deviations of $\bar{\varepsilon}$ smaller than ±10%.
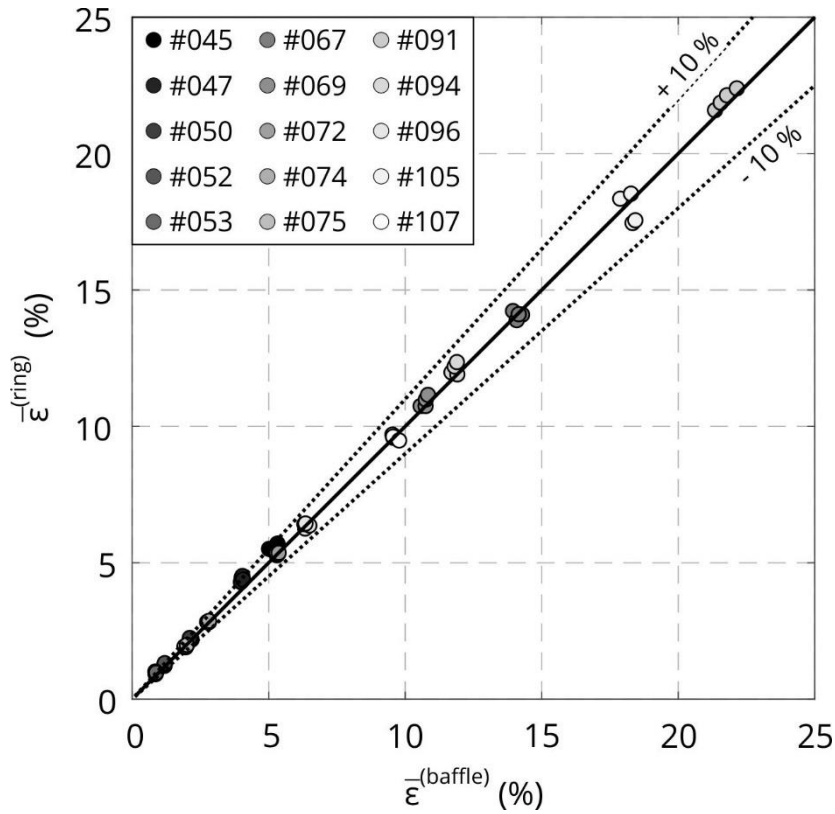
262

263 Figure 4: Parity plot of total gas holdup $\bar{\varepsilon}$ values of the undisturbed two-phase flow at the
264 furthest upstream imaging planes of both flow constrictions.

265

266 The coefficient of variation reveals a maximum deviation value of 7.16% for the
267 lowest gas holdups. This proves undisturbed two-phase flow conditions upstream
268 of the flow constrictions for each operating point, which is an important quality
269 criterion for CFD comparison and allows for the characterization of the flow
270 constriction impact on the flow field excluding operational influences.
271 Furthermore, the result of the initial flow condition comparison proves the
272 reliability of the introduced image data processing procedure.

273

274 *3.1   Gas holdup and phase distribution*

275 Figure 5 exemplarily shows sectional views of the gas fraction through the
276 cross-sectional center of the test section pipe ($-1 \leq x/R \leq 1$ for $y/R = 0$) for both
277 flow constrictions and superficial velocities of $j_l = 0.4050$ m·s^{-1} and $j_g = 0.0368$ m·s^{-1}

278 (#072). In addition, the time-averaged cross-sectional gas fractions $\bar{\varepsilon}_{i,j}$ are shown.

279 The sectional views are perpendicularly arranged to the edge of the baffle-shaped

280 flow constriction and show the linearly interpolated time-averaged gas holdup

281 values obtained at the 18 imaging planes. Such sectional views allow a comparison

282 of both flow constrictions, showing gas accumulations for wide areas of the pipe,

283 especially downstream of the baffle-shaped flow constriction. In contrast, gas is

284 clearly redistributed while passing the blockage, leading to a homogenization of

285 the gas phase distribution far downstream of the flow constriction in case of the
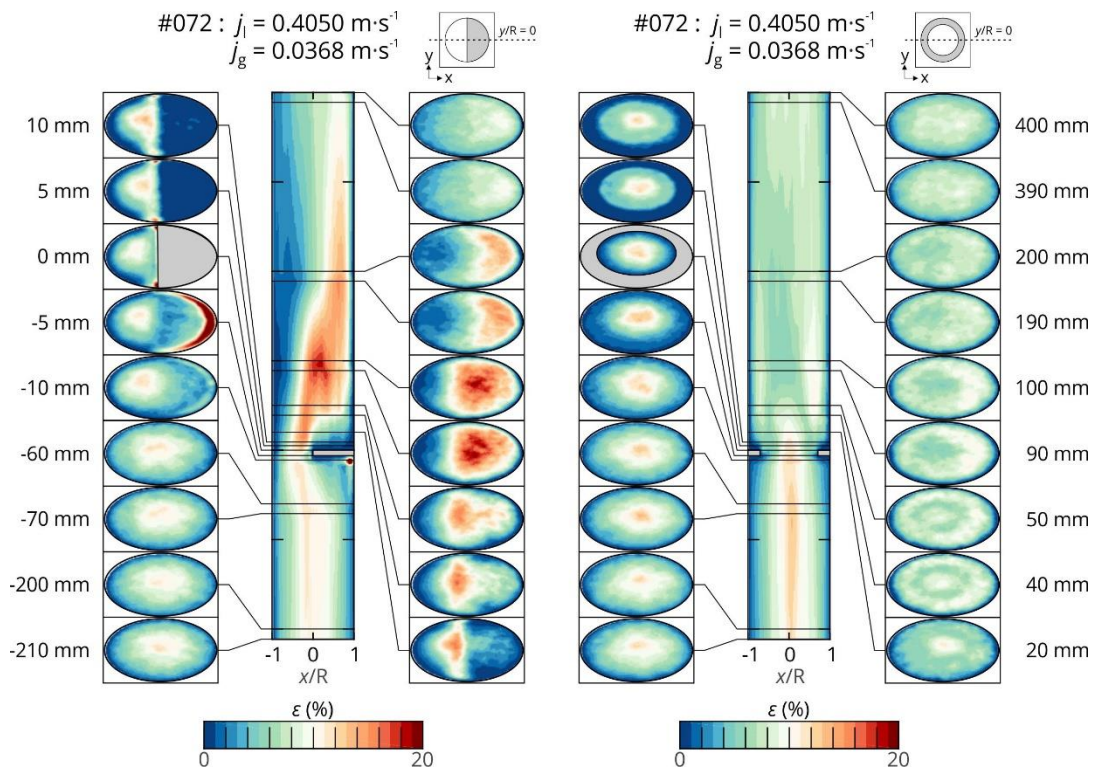
286 ring-shaped type.

287

288 Figure 5:   Time-averaged gas fraction sectional views up- and downstream of the baffle-shaped
289   (left) and ring-shaped (right) flow constriction.

290

291 Another visualization of determined gas holdup values $\bar{\varepsilon}_{i,j}$ is given in Figure 6.

292 Here, each of the sectional views are additionally normalized to its corresponding

293 averaged total gas holdup $\bar{\varepsilon}^{(AB)}$ of imaging planes "A" and "B" that is also indicated

294 at the top of Figure 6. Thus, the color scaling can be interpreted as the relative

15

295 amount of gas phase that is distributed along the test section pipe compared to

296 unaffected flow conditions. Hence, this kind of visualization allows detailed

297 investigations on various operating conditions for a given flow constriction. In

298 Figure 6 results for constant gas superficial velocity of $j_g = 0.0368\,\text{m·s}^{-1}$ and

299 increasing liquid superficial velocities for the baffle-shaped flow constriction are

300 shown.

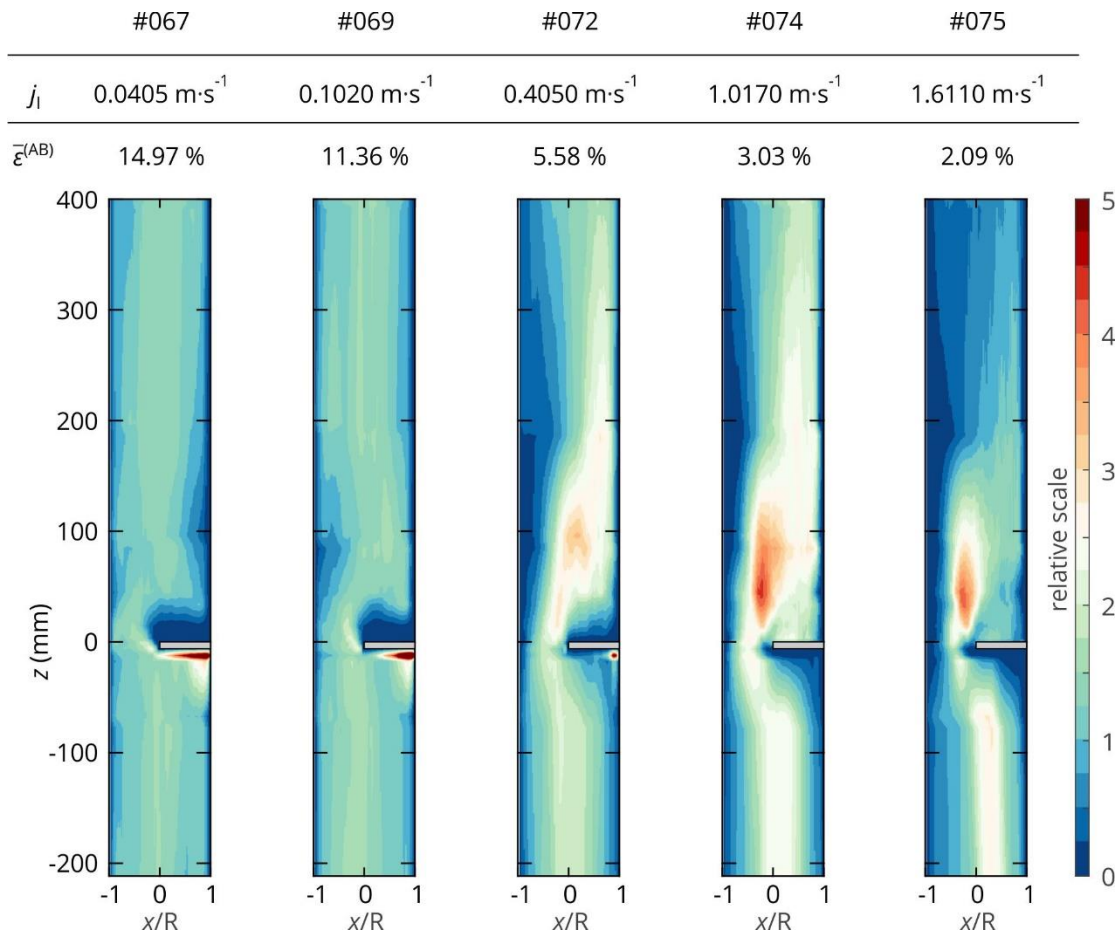|	#067	#069	#072	#074	#075
j_l	$0.0405\,\text{m·s}^{-1}$	$0.1020\,\text{m·s}^{-1}$	$0.4050\,\text{m·s}^{-1}$	$1.0170\,\text{m·s}^{-1}$	$1.6110\,\text{m·s}^{-1}$
$\bar{\varepsilon}^{(AB)}$	14.97 %	11.36 %	5.58 %	3.03 %	2.09 %

301

302 Figure 6: Time-averaged and normalized gas holdup values $\bar{\varepsilon}_{i,j}/\bar{\varepsilon}^{(AB)}$ up- and downstream of the
303 baffle-shaped flow constriction for various superficial liquid velocities j_l and a constant
304 superficial gas velocity of $j_g = 0.0368\,\text{m·s}^{-1}$.

305

306 It can be concluded that all operating conditions provide symmetric flow profiles

307 for the unaffected region upstream of the flow constriction for $z < -60$ mm with a

308 maximum at the pipe center. After that, the influence of the half-sided blockage

309 on the phase distribution becomes more and more evident and leads to gas

accumulations below the flow constriction for the two lowest superficial liquid velocities (#067, #069) since the redirected liquid flow does not provide enough energy to directly transport the gas phase towards the unobstructed side of the pipe. With increasing superficial liquid velocity the gas accumulation below the flow constriction decreases until it is completely vanished for $j_l \geq 1.0170$ m·s^{-1} (#072).

In contrast, gas is accumulated directly downstream of the flow constriction for higher superficial liquid velocities (#072, #074 and #075). This clearly indicates the presence of a recirculation area above the flow constriction that is caused by the strong flow separation at the edge of the flow constriction. For highest superficial liquid velocity $j_l = 1.6110$ m·s^{-1} (#075) a large amount of gas accumulates straight above the edge of the flow constriction, which indicates that the momentum of the recirculated liquid is even high enough to displace gas from the recirculation area back to the pipe center. However, no significant recirculating zone is found for the two lowest superficial liquid velocities (#067, #069). Here, the flow almost immediately re-develops to undisturbed pipe flow conditions, whereas significant asymmetric flow fields are found far downstream of the flow constriction for all other operating conditions (#072, #074 and #075). For the latter, gas is clearly redistributed to the obstructed side of the pipe, which is caused by the lower density of gas that is driven out of the accelerated liquid jet.

A more quantitative comparison is shown in Figure 7, where selected gas holdup profiles from representative imaging planes up- and downstream of both flow constrictions are plotted for the same operating conditions as already depicted in Figure 6. For $z = -200$ mm the comparison of both flow constrictions show similar holdup profiles for all operating conditions, although the overall amount of gas decreases for increasing liquid superficial velocity.

Directly upstream of the baffle-shaped flow constriction at $z = -10$ mm a gas accumulation zone with approximately twice as much gas as at the unobstructed

338   pipe section is found below the blockage for operating conditions #067 and #069.

339   In contrast, almost no gas is found in this area for all other operating conditions.

340   Here, gas is clearly redistributed to the unobstructed pipe section, where a center

341   peak is developed at $x \approx$ -10 mm. However, no significant stagnation zones or gas

342   redistribution are found for the ring-shaped flow constriction. Considering the

343   higher flow velocity due to the acceleration, the gas holdup is expected to decrease

344   close to the ring-shaped flow constriction. However, the profiles provide nearly the

345   same holdup maxima as for z = -200 mm (by respecting the different scaling).

346   Thus, it can be derived that gas is redistributed to the pipe center, where the

347   superimposition of the acceleration and redistribution effect result in

348   approximately constant gas holdup profiles along the centerline of the pipe.
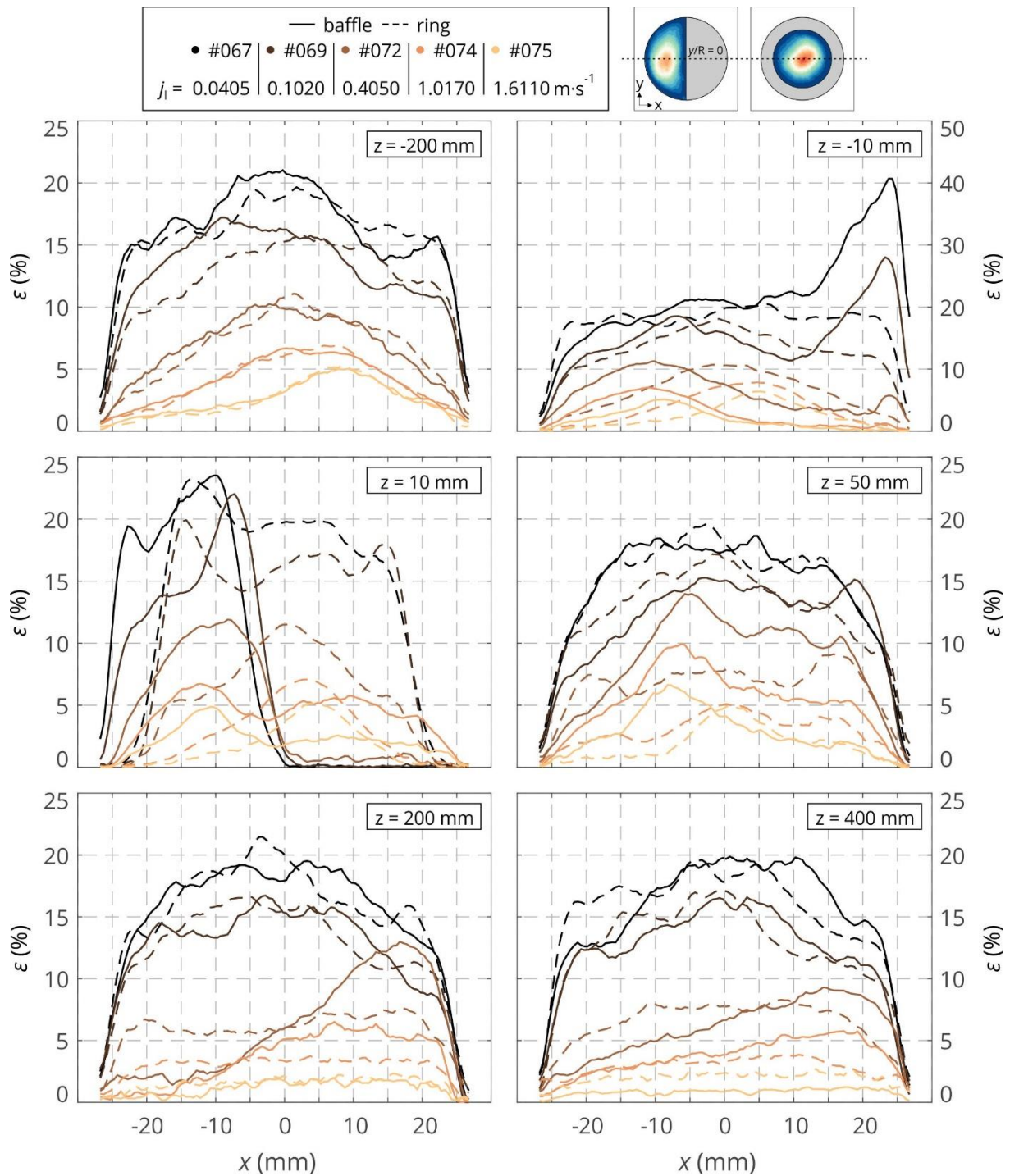
Figure 7: Gas holdup profiles for selected imaging planes up- and downstream of each flow constriction for operating points #067, #069, #072, #074 and #075, showing the effect of increasing liquid superficial velocity j_l.

In the near vicinity downstream of the flow constriction at $z = 10$ mm gas is clearly redistributed towards the unobstructed pipe section for $j_l \leq 1.0170$ m·s^{-1} and baffle-shaped flow constriction. In contrast, the gas holdup profiles show an

357 additional plateau for higher liquid superficial velocities (#074 and #075), due to
358 the recirculating flow in this area. Furthermore, the maxima of the profiles are
359 slightly eccentric towards the edge of the flow constriction with regard to the
360 unobstructed pipe section. In case of the ring-shaped flow constriction the holdup
361 profiles provide a more narrow distribution of the gas in the pipe center as
362 compared to the upstream condition. Here, the expansion of the flow leads to
363 significant lateral movement of the liquid, which in turn drives the gas towards the
364 pipe center due to its lower density.

365 At $z = 50$ mm, the flow re-develops for operating conditions #067 and #069,
366 independent of the flow constriction. On the other hand, the recirculating flow
367 causes a maximum of the holdup profiles between -8 mm $\leq x \leq$ -5 mm for higher
368 liquid superficial velocities (#072, #074 and #075) in case of the baffle-shaped flow
369 constriction. In contrast, not only a center peak, but also two peaks near the pipe
370 wall are found in cases of the ring-shaped flow constriction for operating
371 conditions #072 and #074. The latter are caused by recirculating flow in the wake
372 region of the flow constriction. However, this recirculation is less pronounced than
373 for baffle-shaped type and is furthermore not noticeable for operating point #075.

374 Further downstream at $z = 200$ mm and $z = 400$ mm the gas holdup profiles
375 indicate that the two-phase flow is fully re-developed for operating conditions
376 #067 and #069 for both flow constrictions and no significant redistributions of the
377 gas are noticeable compared to the unaffected upstream conditions. In contrast,
378 the flow seems to be also re-developed for higher liquid superficial velocities
379 (#072, #074 and #075) and the ring-shaped flow constriction, but with a persisting
380 difference in the gas distribution, since no significant peaks are found as in case
381 of unaffected upstream conditions. On the other hand, a clear redistribution of
382 the gas towards the obstructed side of the pipe cross-section is still present for
383 those liquid superficial velocities in case of baffle-shaped flow constriction.

384   Although the peaks decay for increasing relative distances, the flow requires

385   longer distances to re-develop for these operating conditions.

386

387   *3.2   Bubble sizes*

388   The impact of both, baffle-shaped and ring-shaped flow constriction, on bubble

389   sizes and their distribution is shown in Figure 8 for a bubble size class width of

390   Δd_B = 0.5 mm, again for the same operating conditions and imaging planes as

391   described in Figure 6. For better visual interpretation of the results, the bubble size

392   distributions of operating conditions #072, #074 and #075 are additionally shown

393   in the rescaled inset plots. A comparison of the undisturbed two-phase flow at

394   relative distance z = -200 mm reveals no change of the bubble size distribution for

395   both investigated flow constrictions. A most probable bubble diameter of

396   d_B ≈ 6.0 mm can be identified for all cases, which was already observed by

397   Banowski et al. [22]. Thus, on the one hand it can be assumed that the gas injector

398   produces bubbles of comparable size over a wide range of inlet conditions and,

399   on the other hand, that the flow is fully developed for all considered operating

400   conditions. However, even smaller bubbles might be expected for highest liquid

401   superficial velocities, where higher shear forces and thus higher bubble break-up

402   is expected. In the near vicinity upstream of the flow blockage at z = -10 mm the

403   bubble size distribution is similar to the undisturbed upstream flow condition for

404   operating conditions #067, #069 and #072 for both flow constrictions. Slightly

405   larger bubbles are found for operating point #074 and both flow constrictions, as

406   well as operating point #075 in case of the rings-shaped flow constriction. Here,

407   the sudden reduction of the test section pipe leads to increased lateral movement

408   of the two-phase flow and, thus, a redistribution of the gas towards the unblocked

409   pipe cross-section or pipe center in case of baffle-shaped or ring-shaped flow

410   constriction respectively. Thus, bubble coalescence becomes more probable. In

411   contrast, two peaks of the bubble size distribution are found for operating point

21

412   #075 and baffle-shaped flow constriction. Here, the liquid velocity gradients cause

413   high shear forces that additionally split bubbles. The superposition of both effects,

414   break-up and coalescence respectively, lead to most probable bubble sizes of
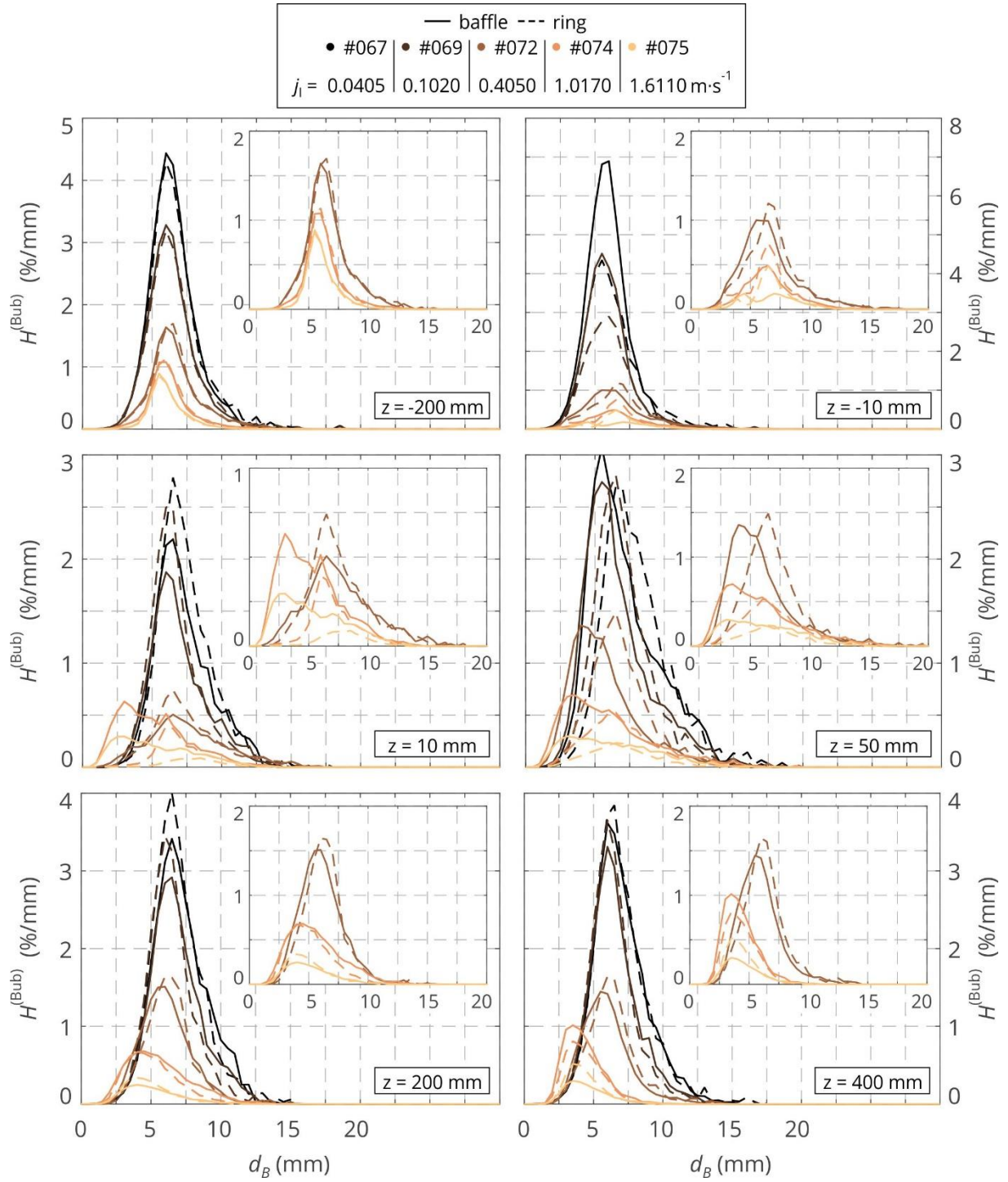
415   4.5 mm and 7.0 mm.

Figure 8: Bubble size distribution as frequency of occurrence $H^{(\mathrm{Bub})}$ for selected imaging planes up- and downstream of each flow constriction for operating points #067, #069, #072, #074 and #075, showing the effect of increasing liquid superficial velocity j_l. For better visual interpretation, insets represent a close-up view of operating points #072, #074 and #075.

Directly downstream of the flow constriction at $z = 10$ mm, the bubble size distribution for operating conditions #067, #069 and #072 shows no significant

425   difference as compared to the undisturbed flow for both flow constrictions.

426   However, slightly higher amount of bubbles with $d_B \leq 4.0$ mm are found in case

427   of baffle-shaped flow constriction and at operating point #072, which are caused

428   by the higher shear of the accelerated flow. Furthermore, the bubble size

429   distribution provides a peak at smaller bubbles of $d_B \approx 3.0$ mm and also a wider

430   distribution for operating conditions #074 and #075 in case of baffle-shaped flow

431   constriction. In contrast, less but larger bubbles are found for the same operating

432   conditions and ring-shaped flow constriction. Thus, the symmetric reduction of the

433   cross-section causes less break-up of bubbles but higher coalescence rates at this

434   relative distance to the flow constriction.

435   At $z = 50$ mm, the recirculation of the flow causes a wider distribution of the

436   bubble sizes, as well as a most probable bubble size of 4.0 mm, 3.5 mm and

437   3.0 mm for baffle-shaped flow constriction and operating conditions #072, #074

438   and #075, respectively. This is an explicit indicator for the complex interaction of

439   break-up and coalescence effects in the recirculation area in the wake of the

440   baffle-shaped flow constriction. Furthermore, the bubble size distribution is

441   slightly shifted towards smaller bubbles for the same three operating conditions

442   in case of the ring-shaped flow constriction, since gas is already redistributed

443   towards the pipe wall and, thus, more bubble break-up occurs. In contrast,

444   operating conditions #067 and #069 show slightly higher amounts of larger

445   bubbles with $d_B = 8.0 \ldots 14.0$ mm for both flow constrictions. Further downstream

446   of the flow constriction ($z = 200$ mm and 400 mm) the bubble size distribution

447   shows no significant changes but a slight increase of larger bubbles for operating

448   conditions #067 and #069 due to the reduced static pressure within the test

449   section. Furthermore, the bubble size distribution for operating point #072 is

450   approximately equal to the undisturbed upstream flow but with slightly smaller

451   most probable bubble size of $d_B \approx 5.5$ mm, also for both flow constrictions. Thus,

452   in terms of bubble sizes the two-phase flow has already re-developed at

453   z = 200 mm, although the gas is still redistributed as shown in Figure 7. In contrast,

454   bubble sizes are further decreased, resulting in a left skewed distribution for

455   operating conditions #074 and #075 in case of both flow constrictions. Here, the

456   high shear forces are still producing higher break-up rates of the bubbles and the

457   flow has not yet reached stable flow conditions.

458   In Figure 9 the bubble size distribution is shown as probability density function

459   (PDF) for all imaging planes and operating points #069 and #074. It shows the

460   development of the bubble size distribution up- and downstream of the

461   baffle-shaped flow constriction. Additionally, the averaged bubble diameter $\bar{d}_B$ is

462   indicated as black vertical line for each distribution. In case of operating point

463   #069, no significant changes of the shape of the bubble size distribution as well as

464   the mean bubble diameter is discovered over the entire test section, which is

465   similar to results of the frequency of occurrence presented in Figure 8. In contrast,

466   a clear impact of the baffle-shaped flow constriction on the bubble size

467   distribution is found for operating point #074. On the one hand, the averaged

468   bubble diameter $\bar{d}_B$ clearly decreases downstream of the flow constriction,

469   verifying the increased bubble break-up also in terms of the PDF. On the other

470   hand, the change of shape from mono- to bi-modal distribution (and vise-versa) of

471   the bubble size in the recirculation zone behind the flow constriction is clearly

472   provable (z = 5...50 mm). Subsequently, bubble sizes of operating point #074 show

473   narrower distributions as compared to operating point #069 for unaffected

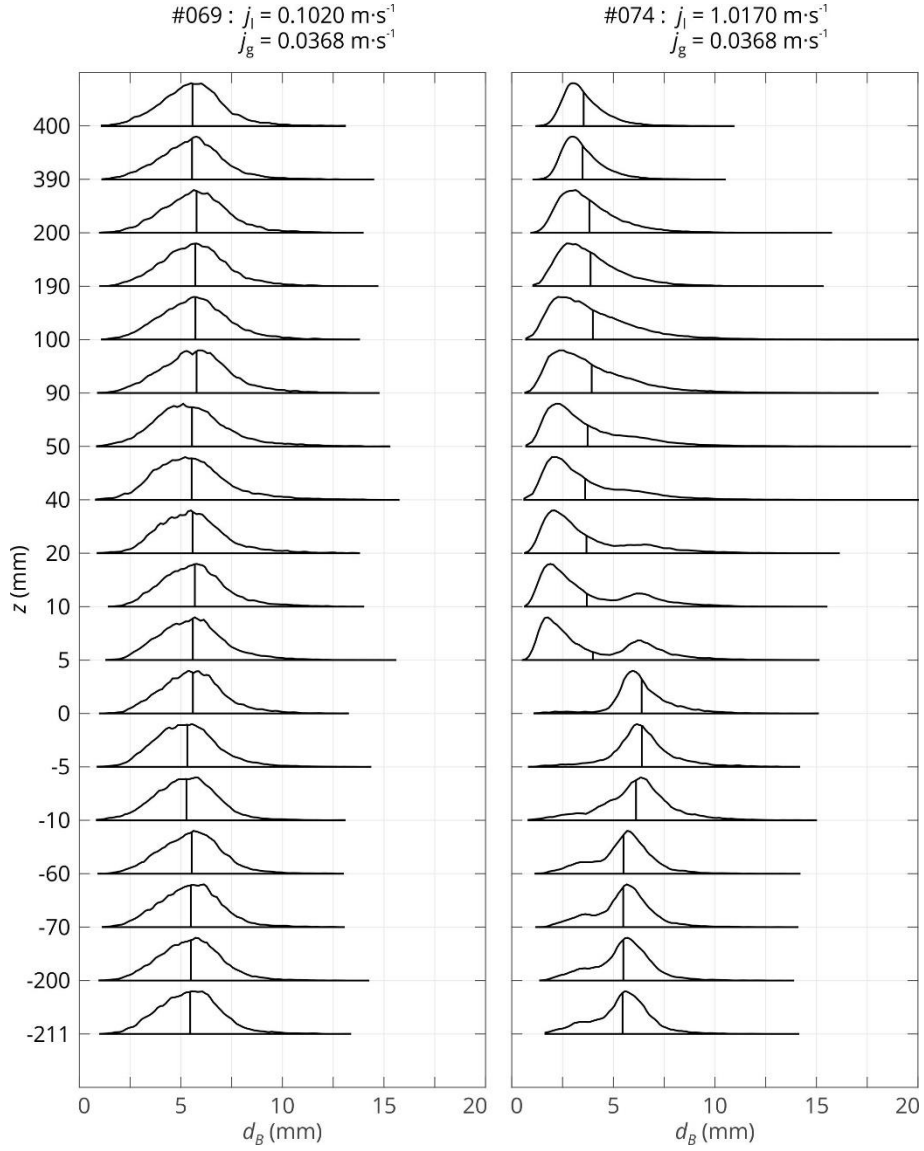474   upstream as well as far downstream flow conditions.

475

Figure 9: Bubble size distribution as probability density function for all imaging planes up- and downstream of the baffle-shaped flow constriction and operating points #069 and #074.

In Table 3, mean bubble diameters for undisturbed flow $\bar{d}_B^{(\text{in})}$ and affected flow $\bar{d}_B^{(\text{out})}$ for both flow constrictions are shown for the same operating conditions as in Figure 8. Here, $\bar{d}_B^{(\text{in})}$ and $\bar{d}_B^{(\text{out})}$ represent the averaged mean diameter of the four upstream imaging planes of scanning positions "A", "B" and of the two downstream imaging planes of scanning positon "I", respectively. Eventually, the change in mean bubble size is defined as $\bar{d}_B^{(\text{ratio})} = \bar{d}_B^{(\text{out})}/\bar{d}_B^{(\text{in})}$. It can be seen, that $\bar{d}_B^{(\text{in})}$ is approximately equal for all operating conditions, whereas $\bar{d}_B^{(\text{out})}$ clearly decreases

26

with increasing liquid superficial velocity. No influence of the flow constriction is recognizable for operating condition #067, where the mean bubble size increases because of the decreased static pressure within the test section. Interestingly, the mean bubble diameter is influenced in the same way for both flow constrictions, despite the different bubble size distributions as discussed for Figure 8.

Table 3: Mean bubble diameter $\bar{d}_B$ for operating points #067, #069, #072, #074 and #075, showing the effect of increasing liquid superficial velocity j_l. The listed values represent averaged data for undisturbed flow upstream $\bar{d}_B^{(\text{in})}$ and affected flow downstream $\bar{d}_B^{(\text{out})}$ of each flow constriction, as well as their ratio $\bar{d}_B^{(\text{ratio})}$.

	baffle-shaped constriction					ring-shaped constriction				
	#067	#069	#072	#074	#075	#067	#069	#072	#074	#075
$\bar{d}_B^{(\text{in})}$	5.68	5.50	5.59	5.49	5.69	5.69	5.54	5.68	5.51	5.69
$\bar{d}_B^{(\text{out})}$	5.83	5.57	4.96	3.52	3.60	5.88	5.58	5.27	3.65	3.72
$\bar{d}_B^{(\text{ratio})}$	1.03	1.01	0.89	0.64	0.63	1.03	1.01	0.93	0.66	0.65

3.3 Lateral bubble velocities

In the following, calculated lateral bubble velocity fields for selected imaging planes up- and downstream of the baffle-shaped flow constriction are discussed for operating conditions #069 (Figure 10) and #074 (Figure 11). Both operating conditions represent two main distinct flow fields that are found in all investigated operating conditions: a) flow fields with gas accumulation upstream of the baffle-shaped flow constriction, but nearly no recirculating flow downstream of it and b) a strong recirculating flow in the wake of the flow constriction for higher liquid superficial velocities. For better visualization, the magnitude of lateral bubble velocity is given by colored image plots, whereas the direction is given by normalized velocity vectors.

510 In Figure 10 the lateral bubble velocity field of operating point #069 with lower
511 liquid superficial velocity of $j_\mathrm{l} = 0.1020\,\mathrm{m\cdot s^{-1}}$ is shown. In case of unaffected
512 two-phase flow at maximum distance upstream of the baffle-shaped flow
513 constriction only low lateral bubble velocity and, thus, lateral movement of the
514 bubbles is found. The velocity vectors point mainly outwards from the center of
515 the pipe because the lateral movement is dominated by bubbles with
516 $d_B < 5.5\,\mathrm{mm}$, which move towards the pipe wall due to the lift force. The lateral
517 movement clearly increases in the direct vicinity upstream of the flow constriction
518 at $z = -10\,\mathrm{mm}$. Here, both radial and azimuthal bubble movement is found, which
519 appears to be counteractive regarding the center plane of the pipe that is
520 perpendicular to the edge of the flow constriction. Following the flow progress, at
521 $z = -6\,\mathrm{mm}$, bubbles mainly move towards the unobstructed pipe section which is
522 also found at the center height of the flow constriction. After passing the flow
523 constriction, two distinct zones with approximately equal lateral bubble velocity
524 are found. The velocity vectors show both movement towards the unobstructed
525 and the obstructed pipe section. Interestingly, both zones are separated by a
526 defined line of zero bubble velocity, which moves from the edge of the flow
527 constriction towards the periphery of the unobstructed pipe section from at
528 $z = 0\,\mathrm{mm}$ to 50 mm, respectively. In this course, bubble movement towards the
529 obstructed pipe section becomes more dominant with a clear maximum at
530 $z = 50\,\mathrm{mm}$. Further downstream, the lateral bubble velocity field shows again
531 unaffected behavior in terms of velocity magnitude and vectors.
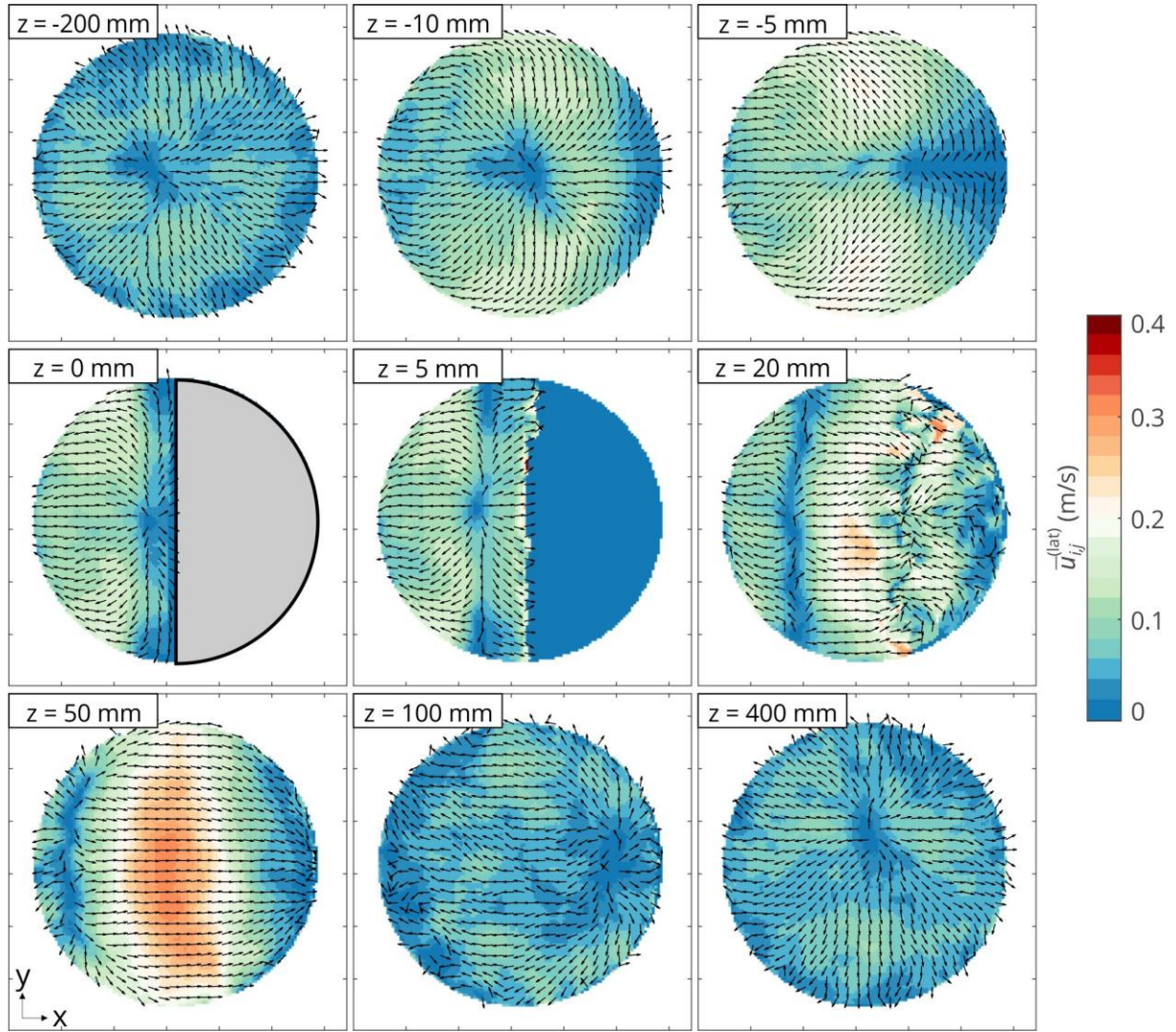
532

533

Figure 10: Lateral bubble velocity fields for selected imaging planes up- and downstream of the
baffle-shaped flow constriction for operating point #069 with j_l = 0.1020 m·s⁻¹ und
j_g = 0.0368 m·s⁻¹. The color scaling shows the magnitude and the arrows show the
velocity vectors of the lateral bubble velocity (velocity vectors are normalized for better
visualization).

In contrast, Figure 11 shows lateral bubble velocity fields for operating point #074
with higher liquid superficial velocity of j_l = 1.0170 m·s⁻¹. Although the lateral
bubble velocity is higher for unaffected two-phase flow at maximum distance to
the flow constriction, the direction of the velocity vectors is comparable to
operating point #069. However, the liquid velocity gradient between center and
wall region is steeper whereby the lateral bubble velocities rise correspondingly.
Close to the flow constriction, the lateral movement clearly increases again.

547 However, in contrast to operating point #069 velocity vectors mainly point towards

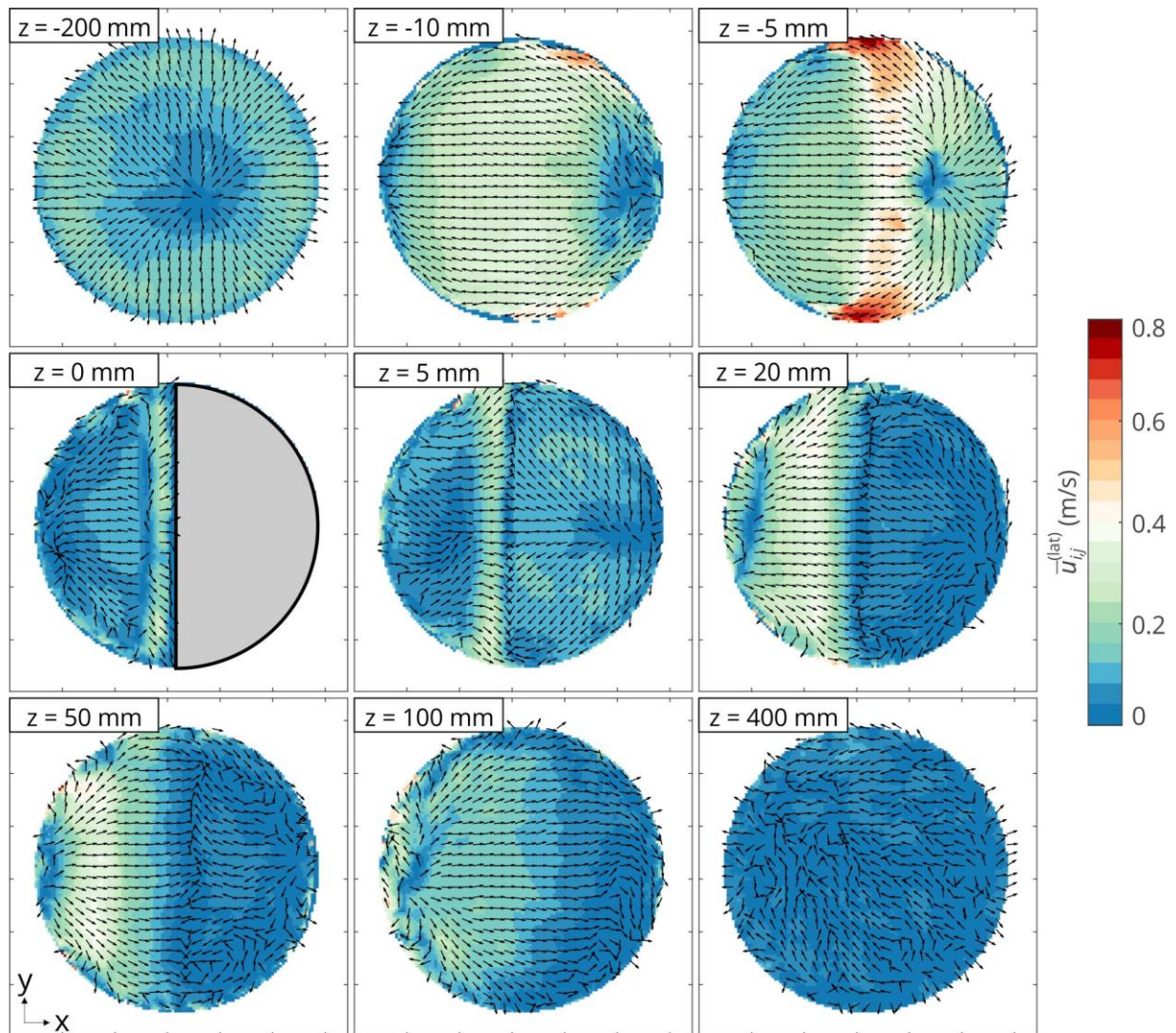548 the unobstructed pipe section with less azimuthal movement.

550 Figure 11: Lateral bubble velocity fields for selected imaging planes up- and downstream of the
551 baffle shaped flow constriction for operating point #074 with $j_l = 1.0170$ m·s^{-1} und
552 $j_g = 0.0368$ m·s^{-1}. The color scaling shows the magnitude and the arrows show the
553 velocity vectors of the lateral bubble velocity (velocity vectors are normalized for better
554 visualization).

555

556 By passing the flow constriction at $z = 0$ mm, only low lateral movement is found

557 and bubbles tend to move to the edge of the flow constriction.

558 In the following downstream wake region from $z = 0$ mm to 50 mm recirculating

559 flow with negative axial liquid velocity is found at the obstructed pipe section. This

560 velocity is, however, lower than for the unobstructed pipe section, which forces

561   bubbles mainly towards the centerline of the pipe straight above the edge of the

562   flow constriction. In contrast, nearly no lateral movement is found in the

563   downward flow, especially at $z = 20$ mm and 50 mm, and the bubble velocity

564   vectors indicate only statistical fluctuations, and, thus, no clear directed

565   movement. At $z = 100$ mm bubbles move towards the obstructed pipe section,

566   which indicates that no recirculating flow affects the lateral movement anymore.

567   Further downstream at $z = 400$ mm, the lateral bubble velocity field shows only

568   statistical movement and rather low velocities of bubbles.

569

4 Conclusion

571   We experimentally studied the two-phase flow around two different flow

572   constrictions using UFXCT imaging technique. A baffle-shaped and a ring-shaped

573   type of flow constriction were used to induce generic three-dimensional flow fields

574   in a vertical DN50 pipe. We studied the flow at various gas and liquid superficial

575   velocities in vertical co-current upward flow under nearly adiabatic conditions.

576   From UFXCT technique phase distributions and bubble sizes were obtained with

577   high temporal and spatial resolution. Therefore, an enhanced data processing

578   procedure was developed to increase the reliability of the image data. The data is

579   available as a benchmark data set at the Rossendorf Data Repository (RODARE)

580   [30,31].

581   In this paper, we exemplarily analyzed flow conditions for the cases of varying

582   liquid superficial velocities and fixed gas superficial velocity of $j_g = 0.0368$ m·s^{-1}. In

583   case of baffle-shaped flow constriction, sectional views of the time-averaged gas

584   holdup revealed the change of gas accumulation from upstream to downstream

585   position with increasing liquid superficial velocity. In case of ring-shaped flow

586   constriction less gas accumulation was found. However, the bubble size

587   distribution as well as the mean bubble diameter showed similar trends along the

588 test section pipe for both flow constrictions. Eventually, lateral bubble velocity

589 fields for the baffle-shaped flow constriction revealed clear lateral movement of

590 the bubbles downstream of the constriction towards the obstructed side of the

591 test section pipe in case of lower liquid superficial velocity. In contrast, nearly no

592 lateral movement was found in this area, but directly upstream of the constriction

593 in case of higher liquid superficial velocity.

594

5 Acknowledgments

6 Nomenclature

Latin letters	
a	offset for calculation of $\bar{\mu}_{i,j}^{(\text{gas})}$
B	single identified Bubble
D and d	diameter (mm)
f	image frequency per scanning plane
F	cross-correlation function
H	frequency of occurrence (%/mm)
j	superficial velocity (m·s^{-1})
L and l	length (mm)
Δm	plane distance map (mm)
N	total number
R	radius (mm)

Δt	time shift (ms)
u	velocity (m·s^{-1})
w	pixel weights
x, y	space coordinates (mm)
z	relative measurement height (mm)
Greek letters	
ε	gas holdup (%)
ε_m	mean value of Gaussian distribution function fitted to gas holdup histogram
μ	attenuation coefficient in (mm^{-1})
μ_μ	mean value of Gaussian distribution
Super- and subscripts	
ax	axial
b	bubble identifier
B	bubble
bin	binarized data set
gas and g	gaseous phase
Id	identifier data set
i, j	space coordinates (pixel)
k	time coordinate (ms)
lat	lateral
liq and l	liquid phase
low and up	scanning plane identifier
ref	reference pixel

tp	two-phase flow data set

600

7 References

[1] D. Bestion, Applicability of two-phase CFD to nuclear reactor thermalhydraulics and elaboration of Best Practice Guidelines, Nucl. Eng. Des. 253 (2012) 311–321. https://doi.org/10.1016/j.nucengdes.2011.08.068.

[2] D. Bestion, The difficult challenge of a two-phase CFD modelling for all flow regimes, Nucl. Eng. Des. 279 (2014) 116–125. https://doi.org/10.1016/j.nucengdes.2014.04.006.

[3] D. Lucas, R. Rzehak, E. Krepper, T. Ziegenhein, Y. Liao, S. Kriebitzsch, P. Apanasevich, A strategy for the qualification of multi-fluid approaches for nuclear reactor safety, Nucl. Eng. Des. 299 (2016) 2–11. https://doi.org/10.1016/j.nucengdes.2015.07.007.

[4] H.-M. Prasser, Evolution of interfacial area concentration in a vertical air–water flow measured by wire–mesh sensors, Nucl. Eng. Des. 237 (2007) 1608–1617. https://doi.org/10.1016/j.nucengdes.2007.02.024.

[5] S. Hosokawa, A. Tomiyama, Multi-fluid simulation of turbulent bubbly pipe flows, Chem. Eng. Sci. 64 (2009) 5308–5318. https://doi.org/10.1016/j.ces.2009.09.017.

[6] D. Lucas, M. Beyer, J. Kussin, P. Schütz, Benchmark database on the evolution of two-phase flows in a vertical pipe, Nucl. Eng. Des. 240 (2010) 2338–2346. https://doi.org/10.1016/j.nucengdes.2009.11.010.

[7] M. Ishii, S.S. Paranjape, S. Kim, X. Sun, Interfacial structures and interfacial area transport in downward two-phase bubbly flow, Int. J. Multiph. Flow. 30 (2004) 779–801. https://doi.org/10.1016/j.ijmultiphaseflow.2004.04.009.

[8] T. Hibiki, H. Goda, S. Kim, M. Ishii, J. Uhle, Axial development of interfacial structure of vertical downward bubbly flow, Int. J. Heat Mass Transf. 48 (2005) 749–764. https://doi.org/10.1016/j.ijheatmasstransfer.2004.07.045.

[9] G. Wang, Z. Dang, P. Ju, X. Yang, M. Ishii, A. Ireland, S. Bajorek, M. Bernard, Experimental study on interfacial structure and interfacial area transport in downward two-phase flow, Int. J. Heat Mass Transf. 106 (2017) 1303–1317. https://doi.org/10.1016/j.ijheatmasstransfer.2016.10.112.

[10] S.K. Wang, S.J. Lee, O.C. Jones, R.T. Lahey, 3-D turbulence structure and phase distribution measurements in bubbly two-phase flows, Int. J. Multiph. Flow. 13 (1987)

630   327–343. https://doi.org/10.1016/0301-9322(87)90052-8.

631   [11]   M. Banowski, U. Hampel, E. Krepper, M. Beyer, D. Lucas, Experimental investigation of
632   two-phase pipe flow with ultrafast X-ray tomography and comparison with state-of-
633   the-art CFD simulations, Nucl. Eng. Des. 336 (2018) 90–104.
634   https://doi.org/10.1016/j.nucengdes.2017.06.035.

635   [12]   Z. Dang, Z. Yang, X. Yang, M. Ishii, Experimental study on void fraction, pressure drop
636   and flow regime analysis in a large ID piping system, Int. J. Multiph. Flow. 111 (2019)
637   31–41. https://doi.org/10.1016/j.ijmultiphaseflow.2018.10.006.

638   [13]   G. Kocamustafaogullari, W.D. Huang, Internal structure and interfacial velocity
639   development for bubbly two-phase flow, Nucl. Eng. Des. 151 (1994) 79–101.
640   https://doi.org/10.1016/0029-5493(94)90035-3.

641   [14]   J.D. Talley, T. Worosz, S. Kim, Characterization of horizontal air–water two-phase flow
642   in a round pipe part II: Measurement of local two-phase parameters in bubbly flow, Int.
643   J. Multiph. Flow. 76 (2015) 223–236.
644   https://doi.org/10.1016/j.ijmultiphaseflow.2015.06.012.

645   [15]   P. Wiedemann, A. Döß, E. Schleicher, U. Hampel, Fuzzy flow pattern identification in
646   horizontal air-water two-phase flow based on wire-mesh sensor data, Int. J. Multiph.
647   Flow. 117 (2019) 153–162. https://doi.org/10.1016/j.ijmultiphaseflow.2019.05.004.

648   [16]   H.-M. Prasser, M. Beyer, T. Frank, S. Al Issa, H. Carl, H. Pietruske, P. Schütz, Gas–liquid
649   flow around an obstacle in a vertical pipe, Nucl. Eng. Des. 238 (2008) 1802–1819.
650   https://doi.org/10.1016/j.nucengdes.2007.11.007.

651   [17]   T. Frank, H.-M. Prasser, M. Beyer, S. Al Issa, Gas-Liquid Flow around an Obstacle in a
652   Vertical Pipe – CFD Simulation & Comparison to Experimental Data, in: 6th Int. Conf.
653   Multiph. Flow, ICMF 2007, Leipzig, 2007: pp. 1–14.

654   [18]   H.-M. Prasser, A. Böttger, J. Zschau, A new electrode-mesh tomograph for gas–liquid
655   flows, Flow Meas. Instrum. 9 (1998) 111–119. https://doi.org/10.1016/S0955-
656   5986(98)00015-6.

657   [19]   H. Pietruske, H.-M. Prasser, Wire-mesh sensors for high-resolving two-phase flow
658   studies at high pressures and temperatures, Flow Meas. Instrum. 18 (2007) 87–94.

659   https://doi.org/10.1016/j.flowmeasinst.2007.01.004.

660   [20]   E. Krepper, M. Beyer, T. Frank, D. Lucas, H.-M. Prasser, CFD modelling of polydispersed

661   bubbly two-phase flow around an obstacle, Nucl. Eng. Des. 239 (2009) 2372–2381.

662   https://doi.org/10.1016/j.nucengdes.2009.06.015.

663   [21]   H.-M. Prasser, M. Misawa, I. Tiseanu, Comparison between wire-mesh sensor and ultra-

664   fast X-ray tomograph for an air–water flow in a vertical pipe, Flow Meas. Instrum. 16

665   (2005) 73–83. https://doi.org/10.1016/j.flowmeasinst.2005.02.003.

666   [22]   M. Banowski, M. Beyer, L. Szalinski, D. Lucas, U. Hampel, Comparative study of ultrafast

667   X-ray tomography and wire-mesh sensors for vertical gas–liquid pipe flows, Flow Meas.

668   Instrum. 53 (2017) 95–106. https://doi.org/10.1016/j.flowmeasinst.2016.02.001.

669   [23]   F. Fischer, D. Hoppe, E. Schleicher, G. Mattausch, H. Flaske, R. Bartel, U. Hampel, An

670   ultra fast electron beam x-ray tomography scanner, Meas. Sci. Technol. 19 (2008)

671   094002. https://doi.org/10.1088/0957-0233/19/9/094002.

672   [24]   F. Fischer, U. Hampel, Ultra fast electron beam X-ray computed tomography for two-

673   phase flow measurement, Nucl. Eng. Des. 240 (2010) 2254–2259.

674   https://doi.org/10.1016/j.nucengdes.2009.11.016.

675   [25]   S. Rabha, M. Schubert, F. Grugel, M. Banowski, U. Hampel, Visualization and

676   quantitative analysis of dispersive mixing by a helical static mixer in upward co-current

677   gas–liquid flow, Chem. Eng. J. 262 (2015) 527–540.

678   https://doi.org/10.1016/j.cej.2014.09.019.

679   [26]   M. Wagner, J. Zalucky, M. Bieberle, U. Hampel, Hydrodynamic investigations of bubbly

680   flow in periodic open cellular structures by ultrafast X-ray tomography, in: 10th Pacific

681   Symp. Flow Vis. Image Process., Naples, Italy, 2015: pp. 15–18.

682   [27]   A.-E. Sommer, M. Wagner, S.F. Reinecke, M. Bieberle, F. Barthel, U. Hampel, Analysis of

683   activated sludge aerated by membrane and monolithic spargers with ultrafast X-ray

684   tomography, Flow Meas. Instrum. 53 (2017) 18–27.

685   https://doi.org/10.1016/j.flowmeasinst.2016.05.008.

686   [28]   Y.M. Lau, F. Möller, U. Hampel, M. Schubert, Ultrafast X-ray tomographic imaging of

687   multiphase flow in bubble columns – Part 2: Characterisation of bubbles in the dense

688   regime, Int. J. Multiph. Flow. 104 (2018) 272–285. 689   https://doi.org/10.1016/j.ijmultiphaseflow.2018.02.009.

690   [29] F. Möller, R. Kipping, C. Lavetty, U. Hampel, M. Schubert, Two-Bubble Class Approach
691   Based on Measured Bubble Size Distribution for Bubble Columns with and without
692   Internals, Ind. Eng. Chem. Res. 58 (2019) 2759–2769.
693   https://doi.org/10.1021/acs.iecr.8b05784.

694   [30] M. Neumann-Kipping, U. Hampel, Hydrodynamic experimental benchmark data of
695   bubbly two-phase pipe flow around a semi-circular constriction, (2019).
696   https://doi.org/10.14278/RODARE.195.

697   [31] M. Neumann-Kipping, U. Hampel, Hydrodynamic experimental benchmark data of
698   bubbly two-phase pipe flow around a ring-shaped constriction, (2019).
699   https://doi.org/10.14278/RODARE.197.

700   [32] A. Schaffrath, A.K. Krüssenberg, F.P. Weiß, E.F. Hicken, M. Beyer, H. Carl, H.M. Prasser,
701   J. Schuster, P. Schütz, M. Tamme, W. Zimmermann, TOPFLOW - A new multipurpose
702   thermalhydraulic test facility for the investigation of steady state and transient two
703   phase flow phenomena, 2001.

704   [33] H.-M. Prasser, M. Beyer, A. Böttger, H. Carl, D. Lucas, A. Schaffrath, P. Schütz, F.-P.
705   Weiss, J. Zschau, Influence of the Pipe Diameter on the Structure of the Gas-Liquid
706   Interface in a Vertical Two-Phase Pipe Flow, Nucl. Technol. 152 (2005) 3–22.
707   https://doi.org/10.13182/NT05-A3657.

708   [34] A. Kak, M. Slaney, Principles of Computerized Tomographic Imaging, IEEE Press, New
709   York, 1988.

710   [35] W.A. Kalender, X-ray computed tomography, Phys. Med. Biol. 51 (2006) R29–R43.
711   https://doi.org/10.1088/0031-9155/51/13/R03.

712   [36] W.A. Kalender, Computed Tomography: Fundamentals, System Technology, Image
713   Quality, Applications, 3rd edn, Publicis Erlangen, Erlangen, 2011.

714   [37] U. Hampel, E. Krepper, D. Lucas, M. Beyer, L. Szalinski, M. Banowski, F. Barthel, D.
715   Hoppe, A. Bieberle, T. Barth, High-resolution two-phase flow measurement techniques
716   for the generation of experimental data for CFD code qualification, Kerntechnik. 78

717   (2013) 9–15. https://doi.org/10.3139/124.110301.

718   [38]   F. Barthel, M. Bieberle, D. Hoppe, M. Banowski, U. Hampel, Velocity measurement for
719   two-phase flows based on ultrafast X-ray tomography, Flow Meas. Instrum. 46 (2015)
720   196–203. https://doi.org/http://dx.doi.org/10.1016/j.flowmeasinst.2015.06.006.

721   [39]   J. Zalucky, T. Claußnitzer, M. Schubert, R. Lange, U. Hampel, Pulse flow in solid foam
722   packed reactors: Analysis of morphology and key characteristics, Chem. Eng. J. 307
723   (2017) 339–352. https://doi.org/10.1016/j.cej.2016.08.091.

724   [40]   M. Bieberle, M. Wagner, F. Gücker, M. Neumann, U. Hampel, Advanced correction
725   algorithms for ultrafast X-ray computed tomography, in: Proc. 9th World Congr. Ind.
726   Process Tomogr., Bath, 2018.

727   [41]   M. Banowski, D. Lucas, L. Szalinski, A new algorithm for segmentation of ultrafast X-ray
728   tomographed gas–liquid flows, Int. J. Therm. Sci. 90 (2015) 311–322.
729   https://doi.org/10.1016/j.ijthermalsci.2014.12.015.

730   [42]   M. Beyer, L. Szalinski, E. Schleicher, C. Schunk, Wire-Mesh Sensor Data Processing
731   Software, (2018) 82. http://mpmt.de/de/produkte/gittersensor/de/downloads/wire-
732   mesh-sensor-data-processing-software (accessed May 11, 2018).

733   [43]   M. Neumann, M. Bieberle, M. Wagner, A. Bieberle, U. Hampel, Improved axial plane
734   distance and velocity determination for ultrafast electron beam x-ray computed
735   tomography, Meas. Sci. Technol. 30 (2019) 084001. https://doi.org/10.1088/1361-
736   6501/ab1ba2.

737   [44]   Y. Taitel, D. Bornea, A.E. Dukler, Modelling flow pattern transitions for steady upward
738   gas-liquid flow in vertical tubes, AIChE J. 26 (1980) 345–354.
739   https://doi.org/10.1002/aic.690260304.

740